Analysis of compressible potential flow over aerofoils using the dual reciprocity method

A. V. G. Cavalieri
P. A. O. Soviero
soviero@pq.cnpq.br
Instituto Tecnológico de Aeronáutica
São José dos Campos
São Paulo, Brazil

ABSTRACT

The use of the linearised potential model for the analysis of compressible flows is quite widespread, and provides good results for subsonic and supersonic flows. However, the calculation of aerofoils and wings subject to transonic flows requires a non-linear model, such as the transonic small-disturbance (TSD) potential equation. The solution of the problem by a singularity distribution requires singularities over the field, as well as panels on the boundary, characterising the procedure known as field panel method. The present work shows results of calculations of the transonic small-disturbance potential equation for flows without shock waves using the dual reciprocity method (DRM), which permits calculation of integrals only at the boundary of the problem, without the need of field distributions. This approach, compared to the field panel methods, takes considerably less computer time, and shows a significant improvement when compared to results of linear theory without much additional computer time, making this technique adequate to design phases of aircraft. Pressure distribution results show good agreement with other methods found in litterature. The low computational cost of the present method allows us to perform parametric tests and explore the effects of thickness and Mach number on the lift and pitching moment coefficients. A discussion of the physical effect of these parameters on the problem is presented, and the thickness of the aerofoil is shown to increase the lift and change the position of the aerodynamic centre. However, this non-linear effect depends on the precise shape of the thickness distribution.

Paper No. 3698. Manuscript received 31 January 2011, revised version received 4 October 2011, accepted 7 October 2011.

https://doi.org/10.1017/S0001924000005285 Published online by Cambridge University Press

NOMENCLATURE

α	angle-of-attack
β	compressibility coefficient,
γ	relation of the specific heats at constant pressure and constant volume
Φ	velocity disturbance potential in the transformed plan
ϕ	velocity disturbance potential
ϕ'	velocity disturbance potential with Riegels correction
c	aerofoil chord
C_L	lift coefficient
C_M	pitching moment coefficient
C_P	pressure coefficient
$C_{L\alpha}$	lift curve slope
C_{Pcrit}	critical pressure coefficient
M_∞	free stream Mach number
t	aerofoil maximum thickness
U_∞	free stream velocity
x_t	position of aerofoil maximum thickness
x_{ac}	aerodynamic centre position
y_s	y co-ordinate of aerofoil surface

1.0 INTRODUCTION

Calculation of subsonic and of supersonic flows over aerofoils and wings by potential methods is possible with a linear theory, which provides accurate results for the pressure distribution. However, transonic flows cannot be modelled by a linear equation, and the linear potential theory, well developed for purely subsonic and supersonic flows, is not capable to describe a transonic flow.

Since Mach numbers of the transonic range are usually commercially interesting for transport aircraft, considerable attention has been given to the study of transonic flows. The use of an approach similar to the panel methods developed by Hess and Smith[1] would be of much importance, since it allows the determination of pressure distribution over bodies of arbitrary geometry without a need of extensive calculations. Panel methods have proven to be useful tools to design aerofoils and wings, with less computer time required than Euler or Navier-Stokes calculations, since only calculations along the surface of the wings (the boundary of the mathematical problem) are required in a panel method formulation.

The work of Spreiter and Alksne[2] is an attempt to solve the non-linear problem which is characteristic of transonic flows. The approach is based on the integral equation, and is similar to the mentioned panel methods. However, the application of Green's theorem to the transonic equation results in an integral equation, with integrals evaluated along the boundary and in the field. The solution of this equation is found by an approximation of the velocity profile along the field, which can reduce the integral in the field to an integral along the boundary. A similar method was developed by Nixon[3], but with a different approximation of the velocity profile.

With faster computers available, a solution to the integral equation with panels in the domain became possible, which resulted on field panel methods. Ribeiro and Soviero[4] presented a field panel method for the solution of the transonic flow over an aerofoil, based on the transonic small-

https://doi.org/10.1017/S0001924000005285 Published online by Cambridge University Press

disturbances equation. The results are valuable; however, much more computer time is required by a field panel method than by a regular panel method.

The field panel method was further developed for more sophisticated applications. Some examples can be found in the works of Houwinck and van der Vooren[5], which present a field panel method based on a low-frequency expression of the unsteady transonic small-disturbances equation; Morino *et al*[6], which show a review of applications of the method for aeroacoustics and aerodynamics, which include unsteady effects and viscous corrections for transonic potential flows; and Gebhardt *et al*[7], which present a field panel method suitable for the design of complex configurations.

Other developments were done by the application of finite-difference, finite-volume and finite-element schemes to the velocity field. A review of the numerical methods for the potential equation for transonic flows can be found in the work of Holst[8]. These methods can provide good predictions of the pressure distributions for transonic flows; however, the required time for calculations is greater than the one for a panel method, an appropriate grid generation should be performed, and artificial viscosity is generally included to provide the convergence of the method.

A transformation of the domain integral to surface integrals is desired if one wishes to decrease the computer time required for the calculation of transonic flows. The appearance of the dual reciprocity method (DRM), presented by Partridge *et al*[9], gives a new alternative for the study of transonic flows. This method allows the calculation with panels distributed only along the boundary of the problem. The application of DRM for aerofoils in transonic flows modelled by the full potential equation was presented in the work of Theurer and Wagner[10], and the same approach was followed by Uhl *et al*[11], which present pressure distributions of wings at transonic speed with good agreement to Euler calculations.

This work focuses on the application of the dual reciprocity method to aerofoils, modeled by the transonic small-disturbances equation. This model is of interest because of its simplicity, since all the singularities are distributed along the chord, and no artifical dissipation needs to be included for the calculations. Also, since the chord is divided into panels, the same discretisation can be used for any aerofoil. Rapid calculations can thus be performed, providing good estimations of the pressures on the aerofoil surface and allowing parametric studies with low computational time.

This paper is organised as follows. In Section 2 we develop the mathematical model for the transonic small-disturbances equation, and introduce the dual reciprocity method to get a formulation for boundary elements. The numerical scheme for the present calculations is presented in Section 3. Validation results are presented in Section 4, and in Section 5 we present parametric studies of the variation of the lift coefficient and in the position of the aerodynamic centre for different aerofoil shapes.

2.0 MATHEMATICAL MODEL

The transonic small disturbances (TSD) equation for a two-dimensional problem can be written as:

$$\beta^2\phi_{xx} + \phi_{yy} = k\phi_x\phi_{xx} \qquad \ldots (1)$$

The present works uses the following expression for k:

$$k = \frac{(\gamma+1)\mathrm{M}_\infty^2}{U_\infty} \qquad \ldots (2)$$

https://doi.org/10.1017/S0001924000005285 Published online by Cambridge University Press

The boundary conditions for Equation (1) are of tangency of the velocities at the surface of the aerofoil. In linearised form, these conditions are expressed as shown below.

$$\phi_y(y=0) = U_\infty \frac{\partial y_s(x)}{\partial x} \quad \ldots (3)$$

By means of a transformation of variables, it is possible to write Equation (1) in a simpler form.

$$X = x \quad \ldots (4)$$

$$Y = \beta y \quad \ldots (5)$$

$$\Phi = \frac{k}{\beta^2}\phi \quad \ldots (6)$$

Application of Equations (4)-(6) in Equation (1) leads to

$$\nabla^2\Phi = \Phi_X \Phi_{XX} \quad \ldots (7)$$

The boundary conditions on the aerofoil surface in the transformed plan are

$$\Phi_Y(Y=0) = \frac{kU_\infty}{\beta^3}\frac{\partial y_s(x)}{\partial x} \quad \ldots (8)$$

At an infinite distance, the boundary conditions are given by zero disturbances. The Kutta condition for a steady flow is assured by the requirement of a constant potential jump at the wake, equal to the potential jump at the trailing edge.

The solution of Equation (7) can be obtained using an integral equation, which results of the application of Green's second theorem. The associated integral equation is:

$$2\pi T\Phi(X_P, Y_P) = -\int \frac{\partial \Phi}{\partial n} G \mathrm{d}\Gamma + \int \Phi \frac{\partial G}{\partial n} + \iint \Phi_X \Phi_{XX} G \mathrm{d}\Omega \quad \ldots (9)$$

The G function in Equation (9) represents the source, the fundamental solution of Laplace's equation. For two-dimensional domains, G is equal to ln r, and r is the distance of the point of interest (X_P,X_P) and the source position. The T coefficient is related to the position of the point P. It is equal to 0 if P is outside the domain, 1 if P is inside and 1/2 if the point is at a smooth part of the boundary, as shown by Hunt[12]. The objective of the dual reciprocity method is the reduction of the double integral of Equation (9) to single integrals. This method is based on an expansion of the right hand side of Equation (7), shown below.

$$\Phi_X \Phi_{XX} = \sum_{j=1}^{n} b_j f_j \quad \ldots (10)$$

In the equation above, f_j represents a set of n appropriate functions, and b_j are constants chosen in order to make the expansion in Equation (10) valid. We define ξ_j functions

$$\nabla^2 \xi_j = f_j \quad \ldots (11)$$

It is then possible to apply Green's theorem with ξ_j, resulting on

https://doi.org/10.1017/S0001924000005285 Published online by Cambridge University Press

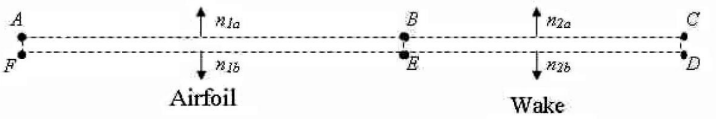


Figure 1. Limiting process for the boundary.

$$2\pi T\xi_j(X_P,Y_P) = -\int \frac{\partial \xi_j}{\partial n} G\mathrm{d}\Gamma + \int \xi_j \frac{\partial G}{\partial n}\mathrm{d}\Gamma + \iint f_j G\mathrm{d}\Omega \qquad \ldots (12)$$

Equation (12) applies for the whole set of functions defined on Equations (10) and (11). Thus, it is possible to write:

$$\sum_{j=1}^{n} 2\pi T b_j \xi_j(X_P,Y_P) = \sum_{j=1}^{n} b_j \left(-\int \frac{\partial \xi_j}{\partial n} G\mathrm{d}\Gamma + \int \xi_j \frac{\partial G}{\partial n}\mathrm{d}\Gamma \right) + \iint \sum_{j=1}^{n} b_j f_j G\mathrm{d}\Omega \qquad \ldots (13)$$

Using the definition of the f_j functions, Equation (13) becomes

$$\sum_{j=1}^{n} 2\pi T b_j \xi_j(X_P,Y_P) = \sum_{j=1}^{n} b_j \left(-\int \frac{\partial \xi_j}{\partial n} G\mathrm{d}\Gamma + \int \xi_j \frac{\partial G}{\partial n}\mathrm{d}\Gamma \right) + \iint \Phi_X \Phi_{XX} G\mathrm{d}\Omega \qquad \ldots (14)$$

A rearrangement of Equation (14) makes possible the transformation of the double integral of Equation (9) to line integrals.

$$\iint \Phi_X \Phi_{XX} G\mathrm{d}\Omega = \sum_{j=1}^{n} 2\pi T b_j \xi_j(X_P,Y_P) + \sum_{j=1}^{n} b_j \left(\int \frac{\partial \xi_j}{\partial n} G\mathrm{d}\Gamma - \int \xi_j \frac{\partial G}{\partial n}\mathrm{d}\Gamma \right) \qquad \ldots (15)$$

With Equations (9) and (15), it is possible to write the potential at the point with only integrals calculated at the boundary of the problem, as shown below:

$$\begin{aligned} 2\pi T\Phi(X_P,Y_P) &= -\int \frac{\partial \Phi}{\partial n} G\mathrm{d}\Gamma + \int \Phi \frac{\partial G}{\partial n}\mathrm{d}\Gamma + \sum_{j=1}^{n} 2\pi T b_j \xi_j(X_P,Y_P) \\ &+ \sum_{j=1}^{n} b_j \left(\int \frac{\partial \xi_j}{\partial n} G\mathrm{d}\Gamma - \int \xi_j \frac{\partial G}{\partial n}\mathrm{d}\Gamma \right) \end{aligned} \qquad \ldots (16)$$

Since the boundary of the domain is the chord, where the conditions of Equation (8) were established, the integrations shown in Equation (16) should be performed along the X axis. For an evaluation of the integrals of Equation (16), the boundary is analysed using a limiting process.

The aerofoil and the wake are considered as rectangular regions, as shown in Fig. 1. Application of Green's second theorem to the regions Ω_A (internal to the aerofoil-ABEF rectangle), Ω_W (internal to the wake-BCDE rectangle) and Ω_O (external to the aerofoil and the wake), after a limiting process with the thicknesses of the aerofoil and the wake approaching zero, leads to:

$$\begin{aligned} 2\pi T\Phi(X_P,Y_P) &= -\int_{S_A} \vec{n}_{1a} \cdot (\nabla\Phi_a - \nabla\Phi_b) G\mathrm{d}\Gamma + \int_{S_A} (\Phi_a - \Phi_b)(\vec{n}_{1a} \cdot \nabla G)\mathrm{d}\Gamma \\ &- \int_{S_W} \vec{n}_{2a} \cdot (\nabla\Phi_a - \nabla\Phi_b) G\mathrm{d}\Gamma + \int_{S_W} (\Phi_a - \Phi_b)(\vec{n}_{2a} \cdot \nabla G)\mathrm{d}\Gamma + \sum_{j=1}^{n} 2\pi T b_j \xi_j(X_P,Y_P) \end{aligned} \qquad \ldots (17)$$

https://doi.org/10.1017/S0001924000005285 Published online by Cambridge University Press

$$+\sum_{j=1}^{n} b_j \left[\int_{S_A} \vec{n}_{1a} \cdot (\nabla\xi_{j_a} - \nabla\xi_{j_b}) \mathrm{d}\Gamma \int_{S_W} \vec{n}_{2a} \cdot (\nabla\xi_{j_a} - \nabla\xi_{j_b}) \mathrm{d}\Gamma \right]$$
$$+\sum_{j=1}^{n} b_j \left[-\int_{S_A} (\xi_{j_a} - \xi_{j_b})(\vec{n}_{1a} \cdot \nabla G) \mathrm{d}\Gamma - \int_{S_W} (\xi_{j_a} - \xi_{j_b})(\vec{n}_{2a} \cdot \nabla G) \mathrm{d}\Gamma \right] \quad \ldots (17)$$

In Equation (17), the *a* subscript indicates that the funcion is evaluated with a limit taken at the upper side of the chord ($Y \to 0+$), and the *b* subscript indicates that the same limit was taken at the lower side ($Y \to 0-$). The integrals are evaluated at the aerofoil chord, S_A, and at the wake, S_W. The limiting process is shown in detail by Cavalieri[13]. Since the f_j functions can be any set that provides an accurate representation of the right hand side of Equation (11), it is possible to choose functions which provide continuity of ξ_j and its derivatives. Consequently, the limits taken at both sides of the chord go to the same value, and Equation (17), with the further assumption that the normal velocity jump at the wake is zero, becomes simpler.

$$2\pi T\Phi(X_P, Y_P) = -\int_{S_A} \vec{n}_{1a} \cdot (\nabla\Phi_a - \nabla\Phi_b) G \mathrm{d}\Gamma + \int_{S_A} (\Phi_a - \Phi_b)(\vec{n}_{1a} \cdot \nabla G) \mathrm{d}\Gamma$$
$$+\int_{S_W} (\Phi_a - \Phi_b)(\vec{n}_{2a} \cdot \nabla G) \mathrm{d}\Gamma + \sum_{j=1}^{n} 2\pi T b_j \xi_j(X_P, Y_P) \quad \ldots (18)$$

This equation allows the calculation of transonic potential flows. It should be noted that the first three integrals of Equation (18) are equal to those of linear potential theory. The first integral corresponds to a distribution of sources along the chord, and the second and third ones to a normal doublet distribution, as shown by Hunt[12]. Thus, the integral equation associated with the transonic small-disturbance equation has an additional term related to the dual reciprocity method. Compared to Equation (9), Equation (18) allows simpler calculations, since the double integral is replaced by a sum of functions calculated at the point of interest.

The pressure coefficient is obtained from the potential using the linearised expression of C_P.

$$C_P = -\frac{2}{U_\infty} \frac{k}{\beta^2} \Phi_X \quad \ldots (19)$$

The equation above can be used for the calculation of the lift and of the pitching moment of the aerofoil. However, since the hypothesis of small perturbations is not valid near the leading edge, a correction based on Riegels formulation[14] should be used in order to correct the velocities and, consequently, the pressure coefficient. This correction, used to determine the pressure distributions, is shown below.

$$U_\infty + \phi'_x = \frac{U_\infty + \phi_x}{\sqrt{1 + \left(\frac{\mathrm{d}y_s}{\mathrm{d}x} \right)^2}} \quad \ldots (20)$$

The present method focus on a numerical solution to the problem. The scheme used for the calculations is described in the following section.

3.0 NUMERICAL SCHEME

The functions f_j employed in the dual reciprocity method can be any set of functions that provides an adequate expansion of the right hand side of Equation (7). Uhl *et al*[11] have proposed the functions

https://doi.org/10.1017/S0001924000005285 Published online by Cambridge University Press

$$f_j = 1 + r_j, \qquad \ldots (21)$$

where r_j is the radius between (X_p, X_p) and a collocation node (X_j, X_j), as the interpolation functions, which are also suggested by Partridge *et al*[9] for several boundary element formulations . This choice is not unique; the simplicity of the chosen functions and the conditioning of the interpolating matrix are the reasons for the definition above.

The f_j functions described in Equation (21) do not tend to zero as the distance goes to infinity. However, for the problems treated in this work the precision of the representation in Equation (10) was sufficient. The obtained error with this set of functions is evaluated for two sample calculations in the Appendix.

Substituting Equation (21) in Equation (11), it is possible to write:

$$\xi_j = \frac{r_j^2}{4} + \frac{r_j^3}{9} \qquad \ldots (22)$$

The ξ_j functions defined above are continuous and have continuous derivatives. Consequently, Equation (18) is valid. The functions in Equation (21) are centred at at set of n nodes distributed along the field. Using the values of $\Phi_X \Phi_{XX}$ calculated at these nodes, it is possible to determine the interpolation coefficients b_j. The definition shown in Equation (10) applied to each node leads to a linear system

$$\begin{bmatrix} \Phi_X \Phi_{XX}(X_1, Y_1) \\ \Phi_X \Phi_{XX}(X_2, Y_2) \\ \vdots \\ \Phi_X \Phi_{XX}(X_n, Y_n) \end{bmatrix} = \begin{bmatrix} f_1(X_1, Y_1) & f_2(X_1, Y_1) & \cdots & f_n(X_1, Y_1) \\ f_1(X_2, Y_1) & f_2(X_2, Y_2) & \cdots & f_n(X_2, Y_2) \\ \vdots & \vdots & \ddots & \vdots \\ f_1(X_n, Y_n) & f_2(X_n, Y_n) & \cdots & f_n(X_n, Y_n) \end{bmatrix} \begin{bmatrix} b_1 \\ b_2 \\ \vdots \\ b_n \end{bmatrix} \qquad \ldots (23)$$

The solution of this system gives the values of b_j. The use of $(1+ r_j)$ as the interpolating functions, instead of simply r_j, simplifies the numerical resolution of the system above, since the main diagonal for $f_j = 1+ r_j$ is not null.

This procedure makes possible the determination of the disturbance potential with an iterative process. The solution based on linear theory is taken as a first guess for the potential. The equation associated to linear theory is presented in Equation (24).

$$\nabla^2 \Phi = 0 \qquad \ldots (24)$$

Solving Equation (24) subject to the boundary conditions of Equation (8) corresponds to finding a homogeneous solution for the problem defined by Equation (7). Some iterations can be performed in order to obtain the non-homogeneous part of the solution. For the iterative process, the following steps are defined:

1. The intensities of the sources and doublets distributed along the chord are calculated according to linear theory. The solution is considered a first guess for the potential in the whole field;
2. The right hand side of Equation (7) is calculated based on the current calculated potential;
3. Values of b_j are calculated solving the system of Equation (23).
4. A new potential can be obtained if the values of b_j are used with Equation (18);
5. This new potential becomes the current one, and steps b-d are repeated until convergence is attained.

https://doi.org/10.1017/S0001924000005285 Published online by Cambridge University Press

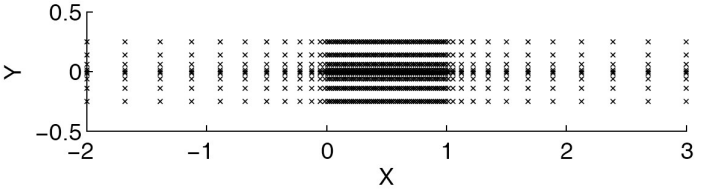


Figure 2. Distribution of the nodes in the field.

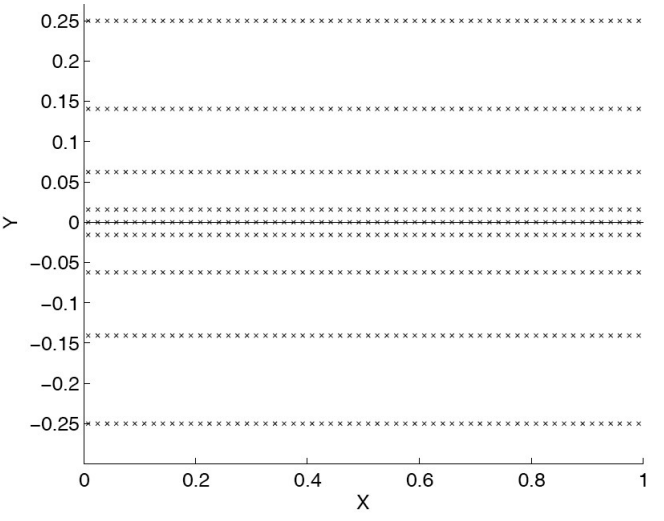


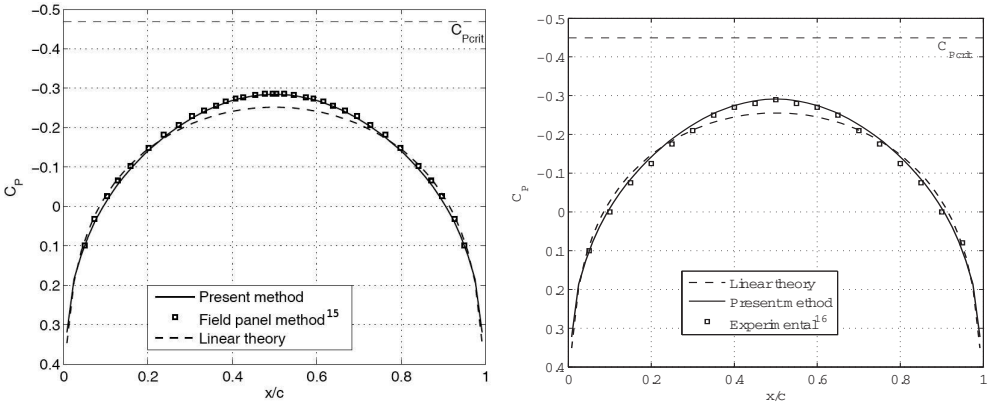
Figure 3. Detail of the distribution near the chord.

If the aerofoil analysed is symmetric, with zero angle-of-attack, the new potentials calculated at Step 4 do not change the velocities at the chord due to the symmetry of the problem. However, the steps above are slightly modificated for the analysis of lifting aerofoils. The potentials obtained at Step 4 do not fulfill the boundary conditions, since normal velocities are induced along the chord. Consequently, the linear solution must be updated at Step 5, with the calculation of new doublet distributions in order to satisfy the boundary conditions. Convergence of the iterative process was typically found after 5-10 iterations for the problems considered in the present work.

Many distributions of nodes were tested. A detailed study of the convergence of the results for a great number of discretisations can be found in Cavalieri[13]. The discretisation used here was the one suggested in that reference, with a division of the chord in 60 panels of equal size and a distribution of 756 nodes in the field. These nodes were distributed quadratically over X from the leading and trailing edges, and also quadratically over *Y*. For values of *X* between 0 an 1, the nodes were distributed over *X* with the same spacing of the panels. This was done to avoid concentration of nodes near the leading and trailing edges, which are regions where the hypothesis of small disturbances is not valid.

The size of the field was also chosen based on the study of the reference above. The width of the field is five times the chord of the aerofoil, and the height is half a chord. Figure 2 shows the position of the nodes across the field, and Fig. 3 shows a detail of the distribution near the chord.

https://doi.org/10.1017/S0001924000005285 Published online by Cambridge University Press



(a) $\alpha = 0°$ and $M_\infty = 0{\cdot}8$ (b) $\alpha = 0°$ and $M_\infty = 0{\cdot}806$

Figure 4. Results for the circular-arc aerofoil.

4.0 RESULTS AND ANALYSIS

The procedure outlined in the previous sections has been applied to the calculations of flows over a symmetrical circular-arc aerofoil, with maximum thickness equal to 6% of the chord. Figure 4(a) shows the comparison of the results of the present method with those of the field panel method of Ribeiro[15].

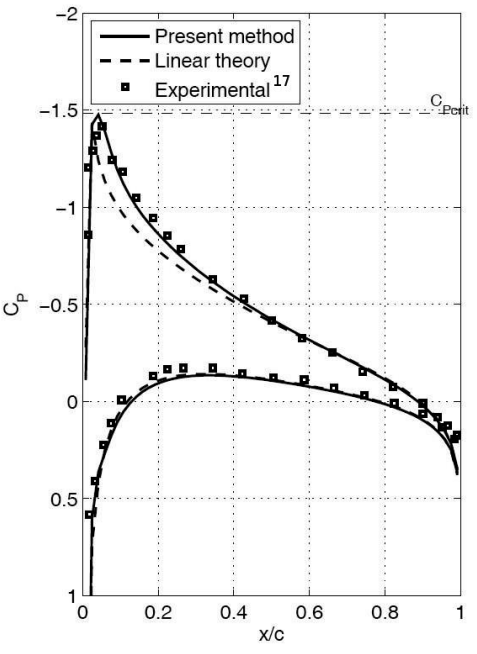
The data show that these two approaches are equivalent, giving almost identical results. However, the calculations performed with the present method took about one tenth of the time required for the field panel method, showing that the dual reciprocity method is a valuable tool for fast calculations.

Figure 4(b) shows a comparison with experimental results of Knechtel[16] for the circular-arc aerofoil. The present method shows a close agreement with the experimental data. It is possible to see that the present method gives better results than the ones by the linear theory at the region where the velocities are higher. At this region, the local Mach number approaches unity, making invalid the assumptions of linear theory. However, in the other regions it is possible to see that the present method, the linear theory and the experimental values almost coincide.

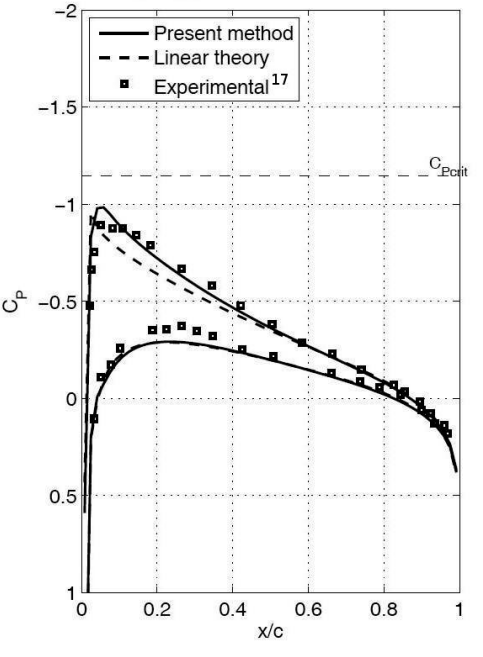
Figures 5(a) and 5(b) show the results of the present method for the NACA 0012 aerofoil, and a comparison with the experimental results of Harris[17]. Again, the results of the present method show good agreement with the experimental values of the pressure coefficient. The pressures at the leading edge predicted by the present method are lower than the ones given by linear theory and are closer to the experimental data at this region. These differences are present only at a small region of the upper surface, where the local Mach number is close to unity; at the rest of the surface the linear theory, the present method and the experimental values are in close agreement.

Figure 6 shows results for the RAE 2822 aerofoil, compared to the values of Theurer and Wagner[10]. That work presents solutions of the full potential equation with the dual reciprocity method. The comparison shows that the present method gives intermediate values between linear theory and the full potential equation. This was expected, since the full potential equation takes all the non-linear terms into consideration. Also, a non-linear expression for the pressure coefficient is used in that work, leading to more negative values of C_P than the ones obtained with the present method (which were calculated with Equation (19), the linear expression of C_P) at the upper surface.

https://doi.org/10.1017/S0001924000005285 Published online by Cambridge University Press



(a) α = 3·16° and M_∞ = 0·6



(b) a = 1·5° and M_∞ = 0·65

Figure 5. Results for the NACA 0012 aerofoil.

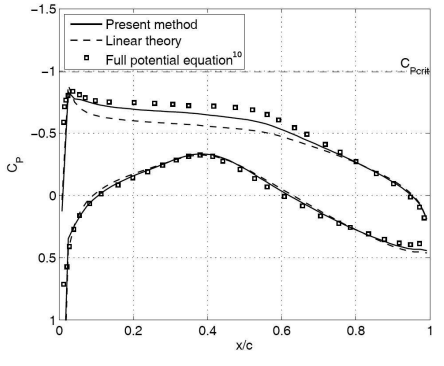


Figure 6. Results for the RAE 2822 aerofoil, with α = 1° and M_∞ = 0·676.

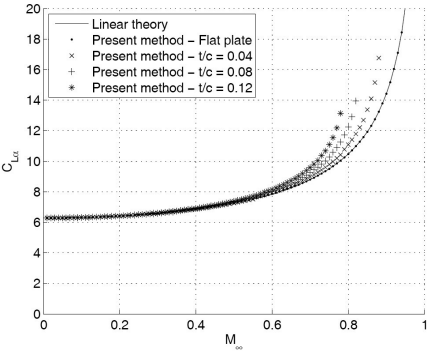


Figure 7. Variation of lift coefficient with Mach number for the circular-arc aerofoil.

For supercritical flows, the convergence of the proposed method is generally not possible. The reason for this divergence may be the ocurrence of shock waves. It is known that the transition from a supersonic velocity for a subsonic one around an aerofoil occurs in most of the cases across a shock wave. Since the chosen f_j functions are smooth, they are probably not appropriate to describe the velocity potentail and its derivatives in the presence of high gradients. Additionally, accurate finite-difference schemes would be necessary. The present method is nonetheless capable of prediction of the pressure distributions for Mach numbers up to the critical value.

https://doi.org/10.1017/S0001924000005285 Published online by Cambridge University Press

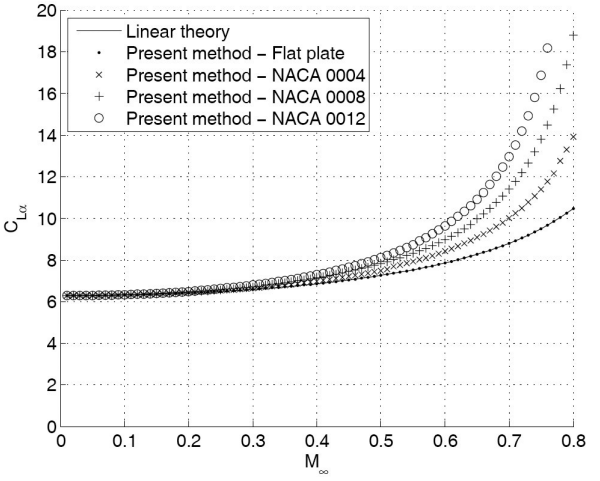


Figure 8. Variation of lift coefficient with Mach number for the NACA 4-digit symmetrical aerofoils.

5.0 PARAMETRIC STUDIES OF THE LIFT AND PITCHING MOMENT COEFFICIENT

With the results for the aerofoils, it is possible to calculate the derivative of the lift coefficient with the angle-of-attack for a wide range of subsonic Mach numbers. The results of $C_{L\alpha}$ as a function of M_∞ are plotted in Figs 7 and 8, relating to, respectively, the circular-arc and NACA 4-digit families. The presented results include the range of Mach numbers where it was possible to obtain convergence of the method.

The difference between linear theory and the present method increases as the Mach number approximates unity. This happens because the non-linear part of Equation (7) has greater magnitudes for higher values of M_∞.

The results presented in Figs 7 and 8 show that the aerofoil thickness increases the lift curve slope for high subsonic Mach numbers. The slope for the flat plate calculated by the present method is equal to the one predicted by linear theory. This is due to an anti-symmetrical field source distribution, which leads to zero induced velocity at the chord for each iteration.

A comparison between a NACA 4-digit and a circular-arc aerofoil is presented in Fig. 9. It is possible to see that for the same maximum thickness (t/c = 0 06), the NACA 4-digit aerofoil has a greater lift curve slope for the higher Mach numbers. This shows that the shape of the thickness distribution has great importance in the calculation of the lift using the TSD equation.

The position of the aerodynamic centre was calculated for the NACA 4-digit and for the circular-arc aerofoil families. The calculations of the lift curve slope and of the position of the aerodynamic centre were done with a linearisation of the lift and the pitching moment coefficients around zero angle-of-attack, using the values of C_L and C_M at 0·1°. The results are shown in Figs 10 and 11.

The results presented in Figs 10 and 11 show that the increase of the Mach number causes a change of the position of the aerodynamic centre, which is no longer at the quarter chord. This change of the aerodynamic centre position is greater for thicker aerofoils.

However, the results of the different aerofoil families have opposite behaviours. While for the circular-arc aerofoils the position of the aerodynamic centre gets closer to the trailing edge for

https://doi.org/10.1017/S0001924000005285 Published online by Cambridge University Press

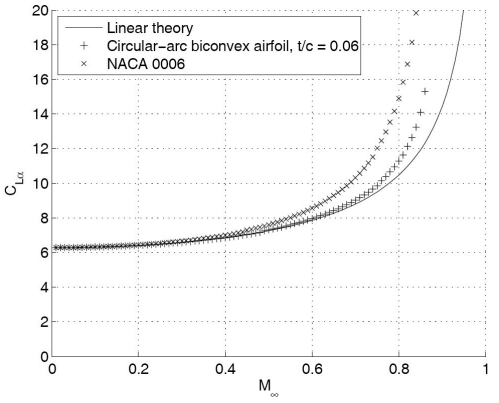


Figure 9. Comparison of the lift coefficients for the circular-arc and NACA 0006 aerofoils.

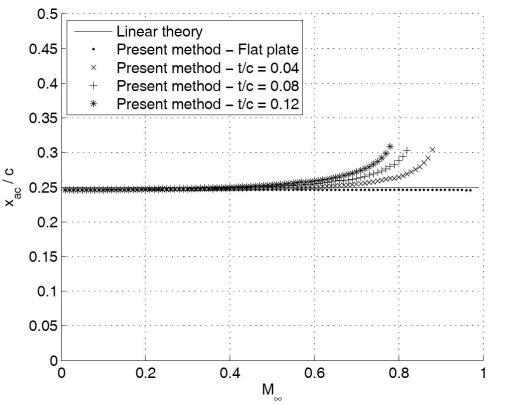


Figure 10. Aerodynamic centre position for the circular-arc aerofoils.

higher Mach numbers, for the NACA 4-digit series the aerodynamic centre becomes closer to the leading edge.

In order to investigate the reason of these effects, some calculations were performed using the extended parabolic aerofoil[14], whose thickness distribution is given by

$$y = a\frac{x(1-x)}{1+bx}, \qquad \ldots (25)$$

where the constants a and b are given by

$$a = \frac{1}{2x_t^2}\frac{t}{c} \qquad \ldots (26)$$

$$b = \frac{1-2x_t}{x_t^2} \qquad \ldots (27)$$

If the position of maximum thickness is equal to 0·5, the aerofoil is equal to a standard biconvex parabolic aerofoil, which, for small thickness, is approximately equal to the symmetrical circular-arc aerofoil.

The results for the lift curve slope for some values of x_t for the extended parabolic aerofoil are shown in Fig. 12. They show that for these aerofoils the variation of the position of maximum thickness has no significant effect in the lift curve slope. However, the results for the position of the aerodynamic centre show different behaviours for each value of x_t/c. This can be seen in Fig. 13.

It is possible to observe in Fig. 13 that for x_t/c equal to 0·4 and 0·6 the aerodynamic centre has a rearward shift for high Mach numbers, while for x_t/c equal to 0·2 there is a forward shift. This difference can be explained with the observation of the pressure distributions presented in Figs 4(a)-6. The non-linear effects are present only at the regions where the velocities approach the speed of sound. This happens at the upper surface of the aerofoil, and the position of the maximum velocity depends on the thickness distribution. The non-linear calculations show that the pressure becomes lower at the region of higher velocity, and remains nearly unchanged at

https://doi.org/10.1017/S0001924000005285 Published online by Cambridge University Press

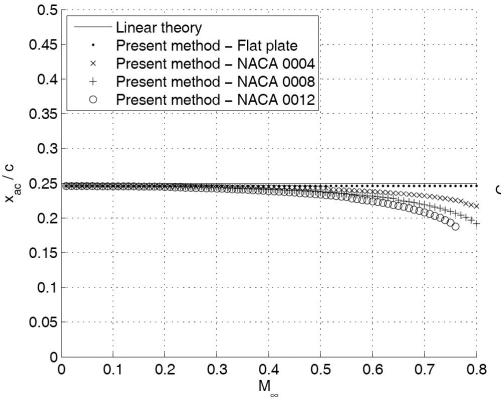


Figure 11. Aerodynamic centre position for the NACA 4-digit symmetrical aerofoils.

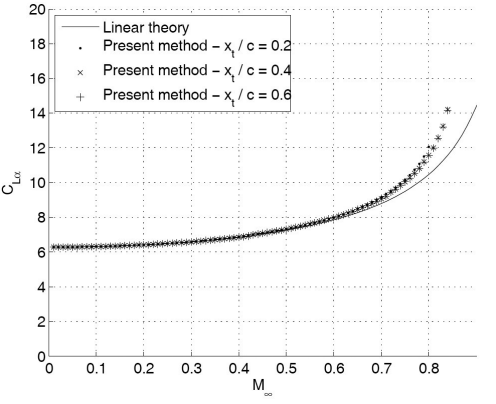


Figure 12. Lift curve slope for the extended parabolic aerofoil.

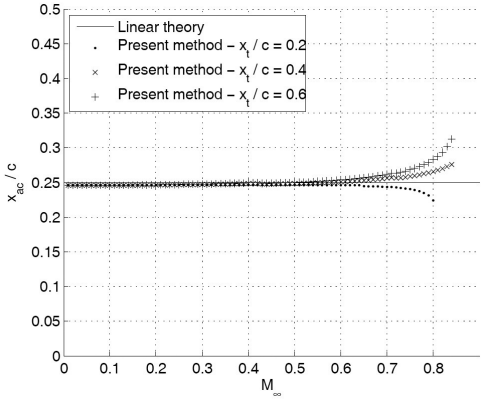


Figure 13. Aerodynamic centre position for the extended parabolic aerofoil.

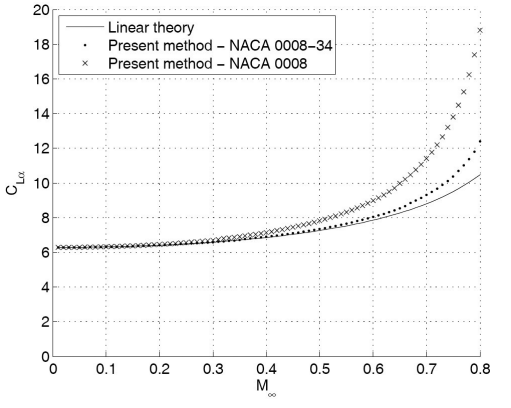


Figure 14. Lift curve slope for the NACA 0008 and NACA 0008-34 aerofoils.

the other regions. Thus, there is a lift increase in the position of maximum flow acceleration. If this position is closer to the trailing edge, this will result in a more negative pitching moment, which is related to a rearward shift of the aerodynamic centre. If the higher velocities are closer to the leading edge, an opposite behaviour happens.

To evaluate these effects in the NACA 4-digit family, Fig. 14 presents the lift curve slope for the NACA 0008 aerofoil and for a modified version (NACA 0008-34), which has a smaller leading edge radius and a different position of maximum thickness, at 40% of the chord.

The results show that the lift increase for higher Mach numbers is greater for the NACA 0008 aerofoil. The thickness distribution of the NACA 0008 induces higher velocities if compared to the NACA 0008-34 section[18]. Thus, the nonlinear effects are stronger at the 0008 section, and consequently the lift is higher.

The position of the aerodynamic centre is shown in Fig. 15. The two analysed aerofoils have opposite behaviours: the NACA 0008 section has a forward shift of the aerodynamic centre, and the NACA 0008-34 has a slight rearward shift. As for the extended parabolic aerofoil, this effect is related to the position of maximum velocity, which is around 7·5% of the chord for the NACA 0008 and near 30% of the chord for the NACA 0008-34 aerofoil[18].

https://doi.org/10.1017/S0001924000005285 Published online by Cambridge University Press

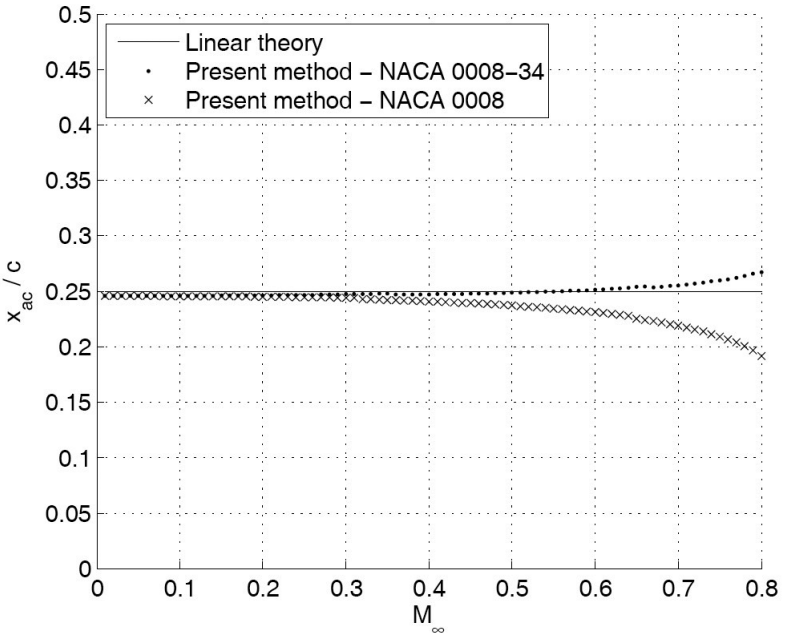


Figure 15. Aerodynamic centre position for the NACA 0008 and NACA 0008-34 aerofoils.

It should be noted that the observed differences from the linear theory are in agreement with experimental results[18], which also show an increase in the lift and a change in the aerodynamic centre position.

6.0 CONCLUSION

Good agreement with experimental data was obtained with the application of the dual reciprocity method for the TSD equation. It should be noted that the formulation presented in this work has a simpler integral equation when compared to the approaches using the full potential equation.

Since a standard calculation can be done in few seconds in an ordinary personal computer, this method is suitable for aerodynamic design, making possible the evaluation of many aerofoil shapes in little time. For example, the calculation of the lift curve slope and the position of the aerodynamic centre as functions of the Mach number, as presented in Figs 7-15, took around 1 minute for each aerofoil. The utilisation of the same discretisation for all the problems requires only one inversion of the matrix of Equation (23) for all the calculations, which simplifies the numerical work, and allows systematic studies, like the work done on the analysis of the effects of thickness in lift and aerodynamic centre position. A perspective for the present method is the extension of the formulation for the three dimensional case of non-linear, compressible flow over a wing, which would still allow calculations with low computational work and parametric studies to explore the effect of the thickness distribution on the lift and the pitching moment.

The results presented here also represent a significant step for unsteady aerodynamics. The method outlined here can also be extended to unsteady problems, modeled by a transonic unsteady equation with small disturbances.

https://doi.org/10.1017/S0001924000005285 Published online by Cambridge University Press

REFERENCES

1. HESS, J. and SMITH, A.M.O. Calculation of potential flow about arbitrary bodies, *Progress in Aerospace Sciences*, 1967, **8**, pp 1–138.
2. SPREITER, J.R. and ALKSNE, A. Theoretical prediction of pressure distributions on nonlifting airfoils at high subsonic speeds, 1954, Tech Rep TR-1217, National Advisory Committee for Aeronautics.
3. NIXON, D. Transonic flow around symmetric aerofoils at zero incidence, *J Aircr*, 1974, **11**, pp 122–124.
4. RIBEIRO, R.S. and SOVIERO, P.A.O. Calculation of transonic flow about airfoils by a field panel method, *Boundary element techniques: Applications in fluid flow and computational aspects*, 1987.
5. HOUWINK, R. and VAN DER VOOREN, J. Improved version of LTRAN2 for unsteady transonic flow computations, *AIAA J*, 1980, **18**, pp 1008–1010.
6. MORINO, L., GENNARETTI, M., IEMMA, U. and SALVATORE, F. Aerodynamics and aeroacoustics of wings and rotors via BEM-unsteady, transonic, and viscous effects, *Computational Mechanics*, 1998, **21**, (4), pp. 265–275.
7. GEBHARDT, L., FOKIN, D., LUTZ, T. and WAGNER, S. An implicit-explicit Dirichlet-based field panel method for transonic aircraf design, 2002, 20th AIAA Applied Aerodynamics Conference, American Institute of Aeronautics and Astronautics.
8. HOLST, T.L. Transonic flow computations using nonlinear potential methods, *Progress in Aerospace Sciences*, 2000, **36**, (1), pp 1–61.
9. PARTRIDGE, P.W., BREBBIA, C.A. and WROBEL, L.C. The dual reciprocity boundary element method, 1992, Computational Mechanics Publications.
10. THEURER, R. AND WAGNER, S. Inviscid transonic flow computation using the dual reciprocity method, *Boundary Element Technology XI*, 1996, pp 13–22.
11. UHL, B., OSTERTAG, J., GUIDATI, G. and WAGNER, S. Application of the dual-reciprocity method to three-dimensional compressible flows governed by the full-potential equation, 1999, 37th AIAA Aerospace Sciences Meeting and Exhibit, Reno, NV, American Institute of Aeronautics and Astronautics.
12. HUNT, B. The panel method for subsonic aerodynamic flow: A survey of mathematical formulations and numerical models with an outline of the new British aerospace scheme, *Computational Fluid Dyn*, 1978, **1**, VKI, Von Karman Inst for Fluid Dyn.
13. CAVALIERI, A.V.G. Calculation of Transonic Flow over Airfoils using the Dual Reciprocity Method (in Portuguese), 2006, Master thesis.
14. SCHLICHTING, H. and TRUCKENBRODT, E. *Aerodynamics of the Airplane*, 1979, McGraw-Hill.
15. RIBEIRO, R.S. Analysis of Transonic Flow by the Method of Singularities (in Portuguese), 1987, Master thesis.
16. KNECHTEL, E.D. Experimental investigation at transonic speeds of pressure distributions over wedge and circular-arc airfoil sections and evaluation of perforated-wall, 1959, Tech Rep TN-D-15, National Aeronautics and Space Administration.
17. HARRIS, C.D. Two-dimensional aerodynamic characteristics of the NACA 0012 airfoil in the Langley 8 foot transonic pressure tunnel, 1981, Tech Rep TM-81927, National Advisory Committee for Aeronautics.
18. ABBOTT, I.H. and VON DOENHOFF, A.E. *Theory of wing sections: including a summary of airfoil data*, 1959, Dover Publications.

APPENDIX

A.1 EVALUATION OF ERRORS AT LARGE DISTANCES FROM THE AEROFOIL

We present in this Appendix an evaluation of the errors of the collocation method using the f_j functions, defined as $1 + r_j$, in model problems. We have solved the linear system of Equation (23) for 51 collocation nodes representing the functions

$$g_1(x) = A\mathrm{e}^{-\frac{x^2}{L^2}} \qquad \ldots (28)$$

https://doi.org/10.1017/S0001924000005285 Published online by Cambridge University Press

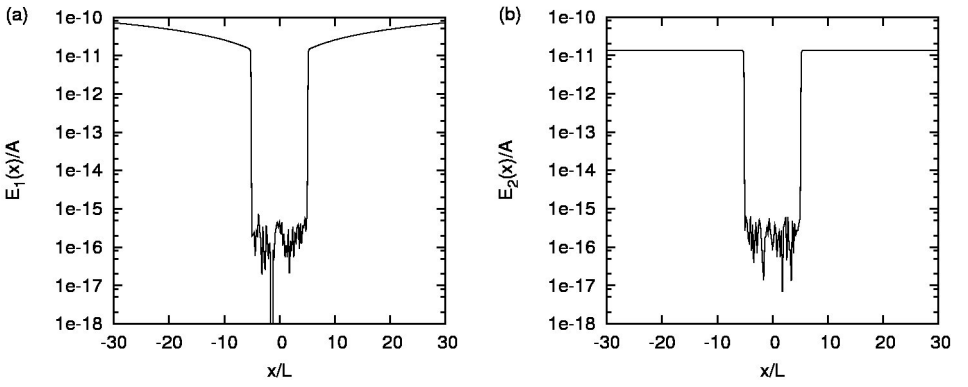


Figure 16. Error of the collocation method for (a) $g_1(x)$ and (b) $g_2(x)$.

and

$$g_2(x) = -A\mathrm{e}^{-\frac{x^2}{L^2}}\mathrm{Sin}\left(\frac{x}{L}\right) \quad \ldots (29)$$

as

$$g(x) = \sum_{j=1}^{n} 1 + r_j(x). \quad \ldots (30)$$

Both functions tend to zero for high $|x|$, and are non-zero in a region with characteristic length L, with maximum amplitude A. They can be seen as possible shapes of the non-linear term $\Phi_X \Phi_{XX}$ along a horizontal line in the computational domain for the present method. The g_1 function is a Gaussian, and g_2 is a sine modulated by a Gaussian; this last function is a simplified model for the acceleration upstream of the profile and the deceleration close to the trailing edge.

The nodes were distributed between $-5L$ and $5L$. To evaluate the errors at large distances from the centre of the domain, we have calculated the approximations of g_1 and g_2 using the Equation (30) for values between $-30L$ and $30L$. The error

$$E_i(x) = \left| \left(\sum_{j=1}^{n} 1 + r_j(x) \right) - g_i(x) \right| \quad \ldots (31)$$

is plotted in Fig. 16.

We notice that for x between $-5L$ and $5L$, i.e. the region where the collocation nodes were distributed, the normalised error is very low. Outside of this region the error becomes higher, but is still at least ten orders of magnitude below the maximum amplitude of g_1 and g_2. Therefore, although the proposed f_j functions do not strictly satisfy the boundary conditions of zero velocity disturbance at infinity, the resulting error is small.

https://doi.org/10.1017/S0001924000005285 Published online by Cambridge University Press